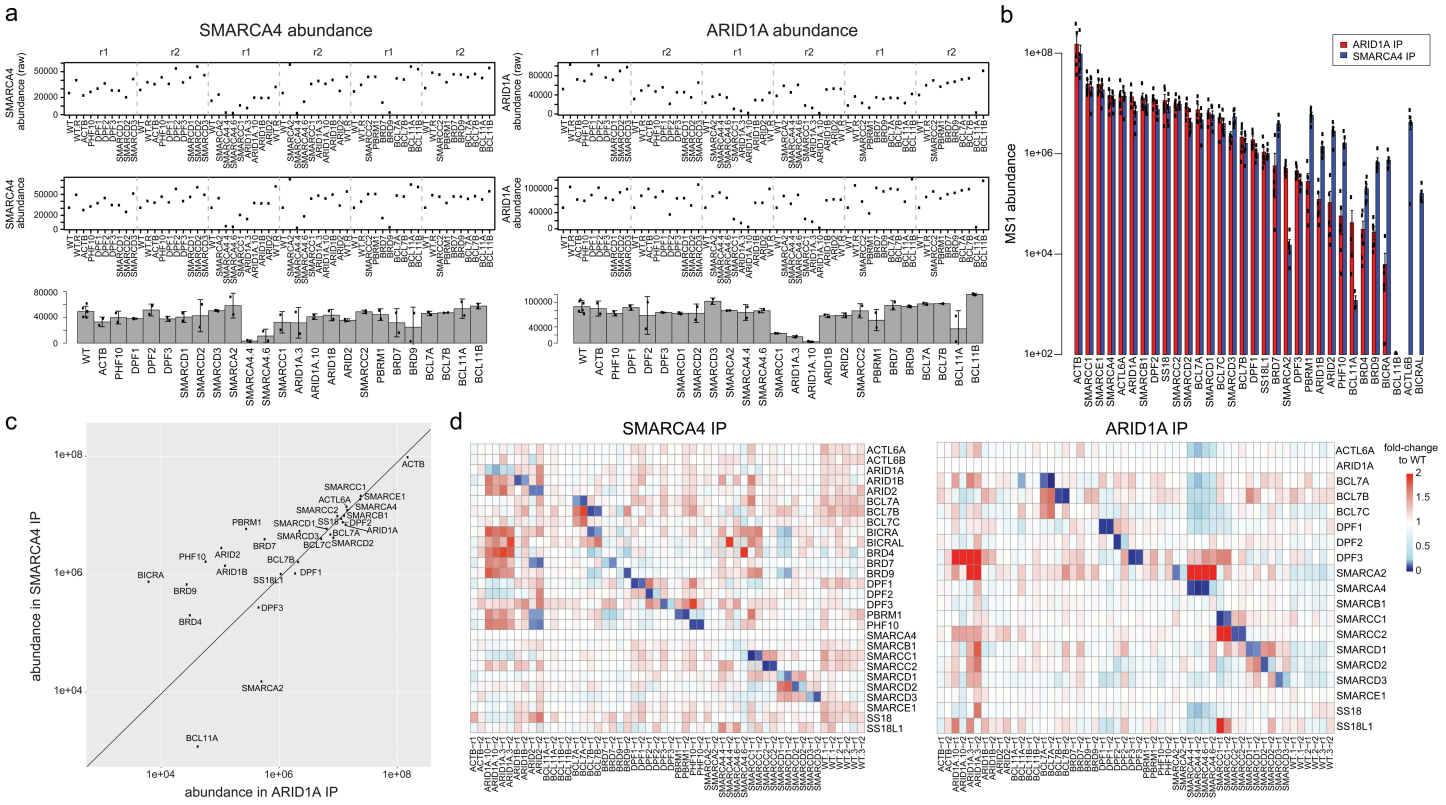

Supplementary Figure 1

IP-MS for BAF subunits across the different HAP1 knock-out cells.

(a) SMARCA4 abundance in SMARCA4 IPs (left) and ARID1A abundance in ARID1A IPs (right) are shown for all samples for n = 2 (n = 6) biologically independent experiments for each KO (WT). Top panel shows unnormalized abundances, middle panel shows the abundances corrected across the different TMT ten-plexes, lowest panel displays average abundance for replicates (mean ± SD). (b) Abundance of BAF members in ARID1A IP-MS and SMARCA4 IP-MS are shown in HAP1 WT cells in a bar graph (mean ± SD, n = 6 biologically independent experiments). (c) Same as in (b), but displayed in a scatter plot. (d) Heatmap showing enrichment of BAF subunits in SMARCA4 IP (left) and ARID1A IP (right) in the different HAP1 knock-out cells relative to their enrichment in HAP1 WT cells displayed for each replicate separate.

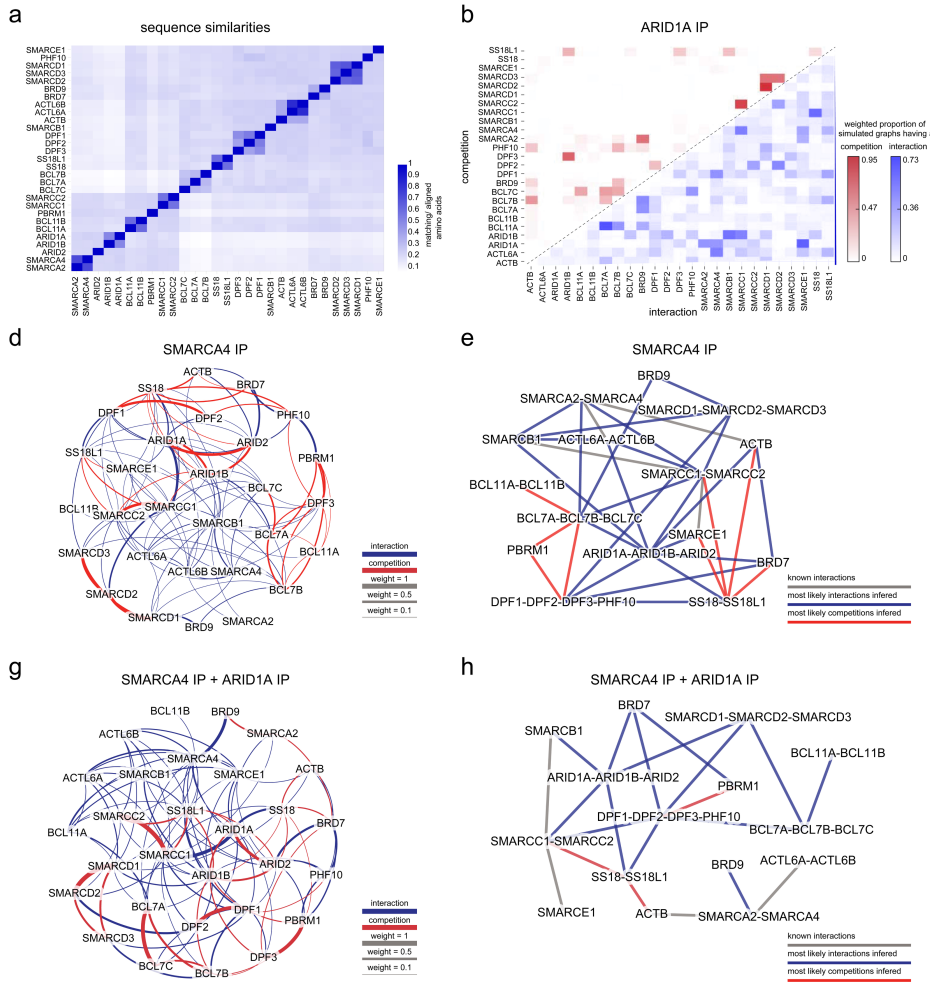

Supplementary Figure 2

Computational structure analyses from IP-MS data.

(a) Calculated amino acid sequence similarities across the different BAF subunits. (b) Weighted frequencies of all pairwise interactions (blue) or competitions (red) between the subunits of the BAF complex as inferred from simulations based on the ARID1A IP-MS data. The weight of an interaction (competition) is given by the normalized sum of the fitnesses of all simulated graphs in which it was observed. (c) Same as in (b), but based on the SMARCA4 IP-MS data. (d) Weighted frequencies of all pairwise interactions (blue) or competitions (red) between subunits of the BAF and PBAF complexes as inferred from simulations based on the SMARCA4 IP-MS data. The weight of an interaction (competition) is given by the normalized sum of the fitnesses of all simulated graphs in which it was observed. A cut-off of weight >0.1169 was used, corresponding to the minimal weight at which all subunits form a single connected graph. (e) Putative organization of the BAF and PBAF complexes obtained by combining interactions and competition classes with direct experimental evidence and most likely interactions inferred from simulations (cut-off of weight >0.17 to result in a single connected graph and only allowing one unique interaction or competition between two nodes). (f) Same as in b), but based on the ARID1A and SMARCA4 IP-MS data. (g) Same as in d), but based on the ARID1A and SMARCA4 IP-MS data (cut-off of weight >0.1216). (h) Same as in e), but for SMARCA4 and ARID1A IP (cut-off of weight >0.257388).

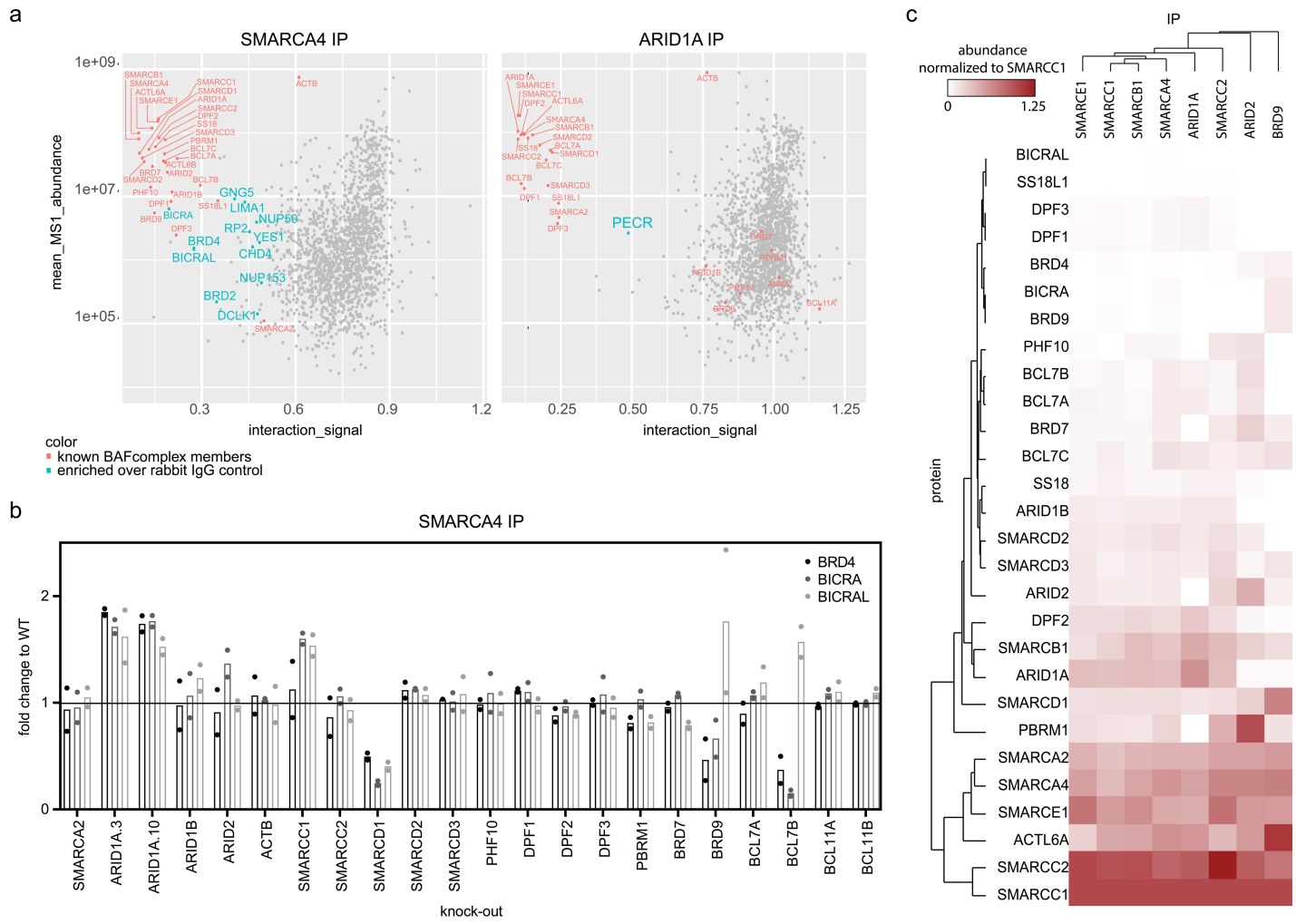

Supplementary Figure 3

IP-MS of BAF subunits reveals new interaction partners.

(a) Scatterplot showing a measure of association with BAF complexes (x-axis) versus abundance (y-axis) of BAF complex members (red) or other proteins (blue) in SMARCA4 IP (left) and ARID1A IP (right). (b) BRD4, BICRA and BICRAL enrichment in SMARCA4 IP across different HAP1 knock-out cells (x-axis; KO subunit is indicated) relative to WT. Bars display mean of two biologically independent experiments. (c) Enrichment of BAF complex members after pulldown of different BAF subunits (x-axis). Abundances normalized to SMARCC1 are shown after mass spectrometry analyses. UPGMA method was used for clustering with Euclidean distance measure.

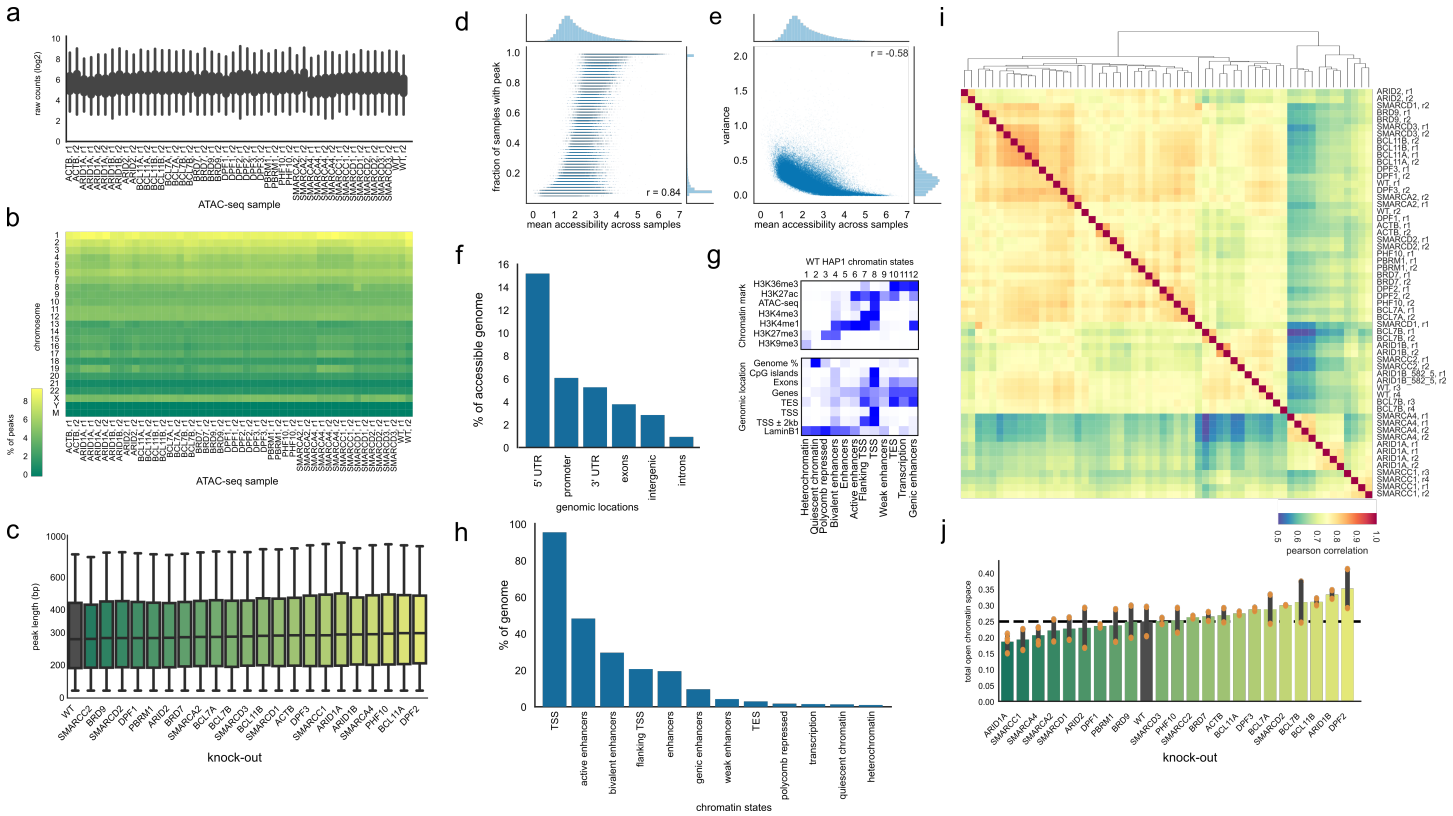

Supplementary Figure 4

Chromatin is preferentially accessible at regulatory regions.

(a) Raw read count distribution across the different ATAC-seq samples. (b) Percentage of ATAC-seq peaks in the different chromosomes for the different KO samples (x-axis; KO is indicated). (c) Distribution of ATAC-seq peak lengths in the different HAP1 cells. (d) Scatter plot of fraction of peak occurrence across all samples within the merged consensus peak set and mean accessibility of the regions across all ATAC-seq samples. Plots on top and right show a histogram of the distributions. (e) Scatter plot of variance and mean accessibility of each regulatory element in the merged consensus peak set across all ATAC-seq samples. (f) Distribution of the consensus peak set in genomic features. (g) Learned chromatin states (x-axis) from ChIP-seq signal and their enrichment in the chromatin marks that gave rise to them (upper panel) or in genomic features (lower panes). (h) Distribution of the consensus peak set in chromatin states specific to the HAP1 cell line. (i) Pairwise Pearson correlation of ATAC-seq samples on the chromatin accessibility signal in the consensus peak set (n = 145,536). (j) Total open chromatin space defined as the sum of peak length. Center values represent the mean and error bars the 95th confidence interval of the mean. n = 2 biologically independent experiments (for ARID1A^{KO} and SMARCA4^{KO} two independent clones were combined). For panels (a) and (c), boxplots represent the 25th, 50th (median) and 75th percentiles, and whiskers represent values 1.5 times below or above the interquartile range. For all boxplots, the full consensus set of accessible chromatin regions were used (n = 145,536). For panels d) and e), the Pearson correlation coefficient was calculated and all regions were displayed (n = 145,536). All panels are the result of at least two biologically independent experiments.

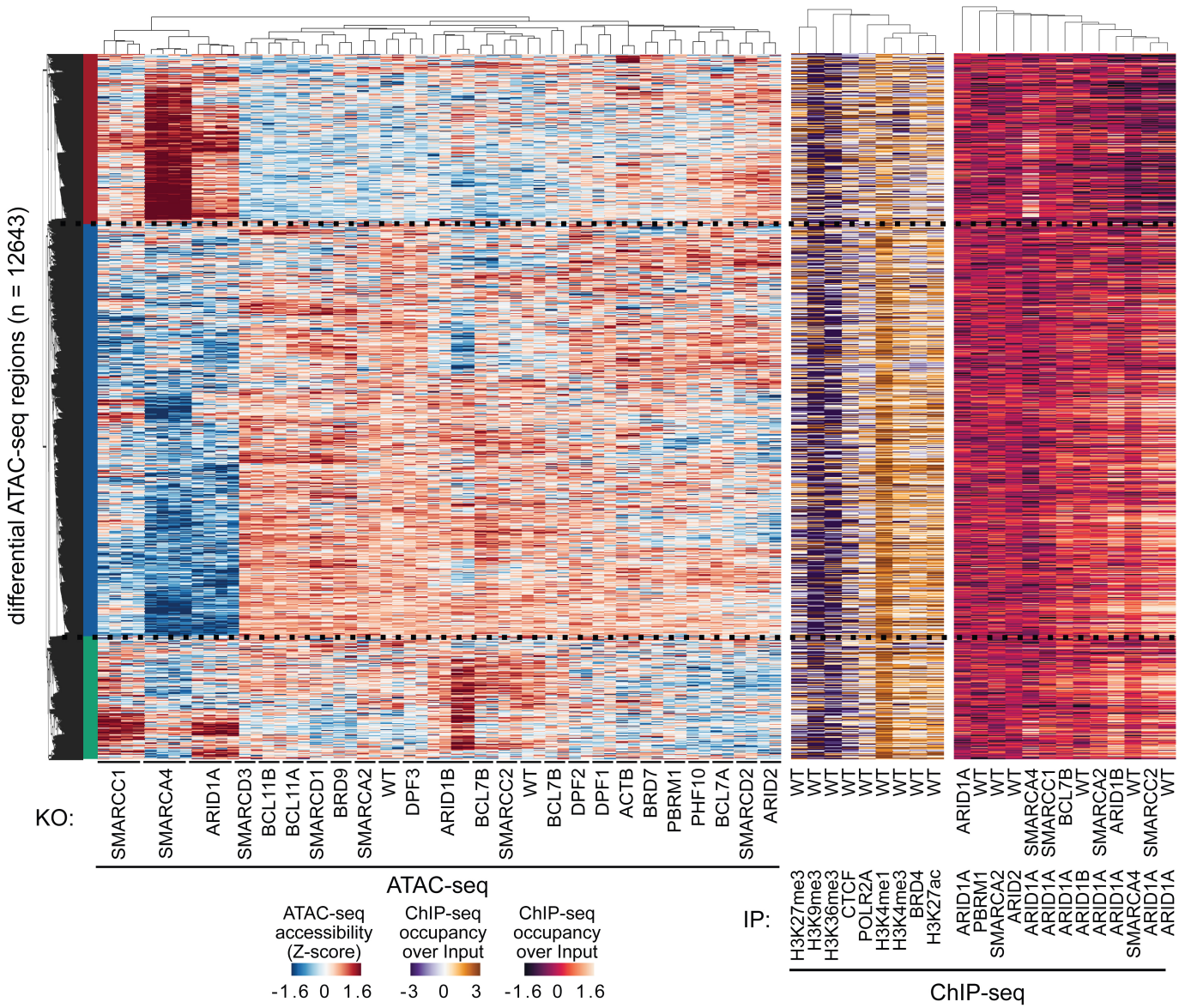

Supplementary Figure 5

Chromatin features of differential accessible regions.

Left panel: Clustering of samples and regions significantly different between any KO compared to WT ATAC-seq data. Hierarchical clustering was performed with Pearson correlation as distance measure between accessibility values transformed with a Z-score per row. Middle panel: ChIP-seq enrichment for histone marks (H3K4me1, H3K27ac, H3K4me3, H3K27me3, H3K9me3, H3K36me3) as well as other factors (Polymerase II (POLR2A), BRD4, CTCF) at differential ATAC-seq regions in HAP1 WT cells. Right panel: ChIP-seq enrichment for BAF complex member (ARID1A, ARID1B, ARID2, SMARCA2, SMARCA4, PBRM1) in HAP1 WT or knock-out cells.

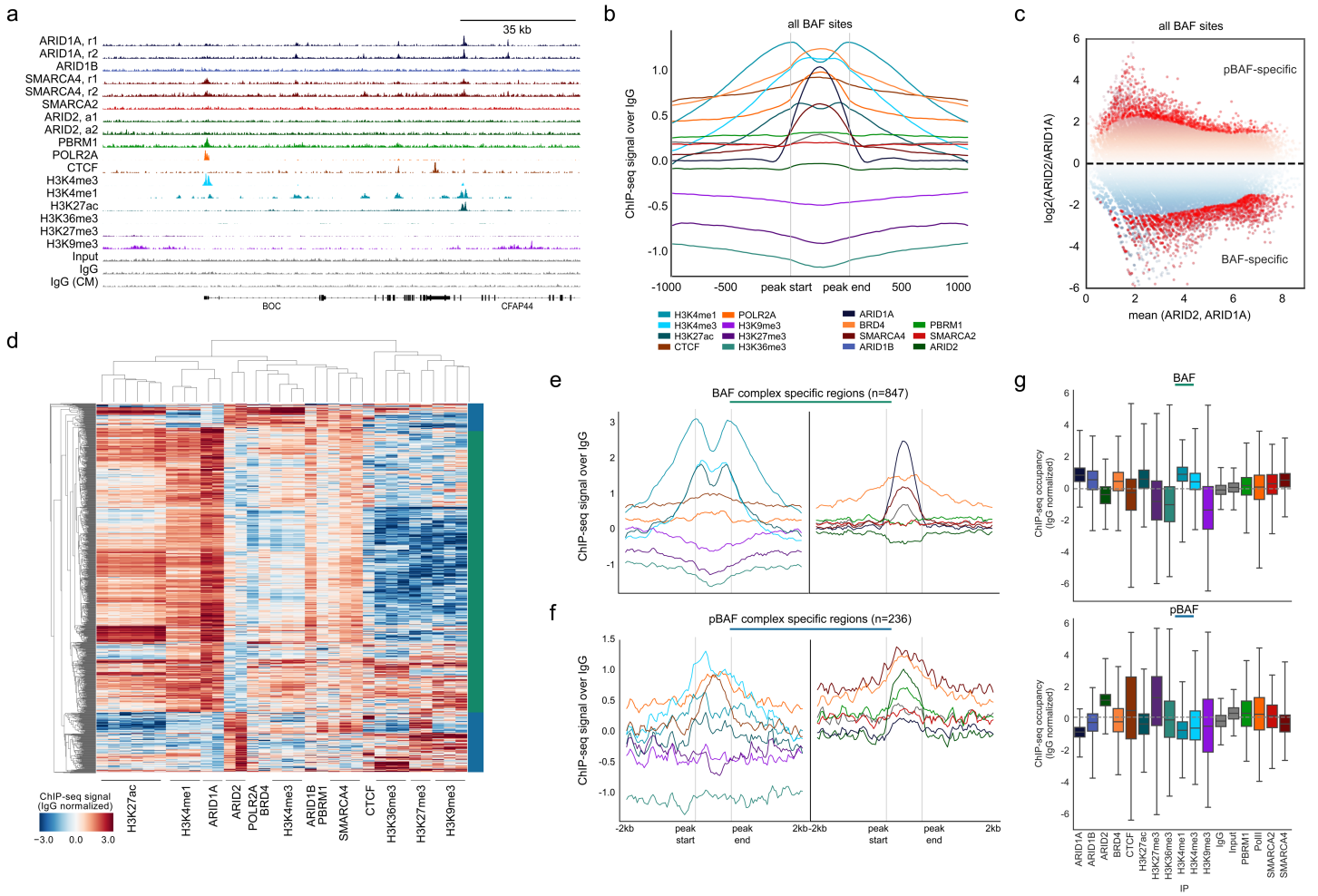

Supplementary Figure 6

BAF and PBAF complexes occupy different genomic loci.

(a) Genome browser tracks for ChIP-seq data in HAP1 wild-type cells. When replicate number is not indicated, tracks represent the merged signal of three biologically independent experiments with the exception of CTCF and POLR2A (n = 1), H3K27me3 (n = 2) and H3K27ac (n = 6). (b) ChIP-seq enrichments around BAF-binding sites. (c) Scatter plot of mean and $\log_2$ fold-change of ARID2-ARID1A signal used to define differentially bound PBAF and BAF sites. (d) Heatmap of BAF and PBAF-specific bound sites showing IgG-normalized ChIP-seq signal for BAF members, histone modifications, Polymerase II (POLR2A), BRD4 and CTCF. Hierarchical clustering with Pearson correlation as distance metric was used. (e) Enrichment of ChIP-seq signal around BAF-specific binding sites. (f) Enrichment of ChIP-seq signal around PBAF-specific binding sites. (g) Occupancy of different factors or histone marks at BAF-specific binding sites (top) or PBAF-specific binding sites (bottom). Boxplots represent the 25th, 50th (median) and 75th percentiles, and whiskers represent values 1.5 times below or above the interquartile range across ChIP-seq replicates in BAF (n = 847) or pBAF-specific sites (n = 236).

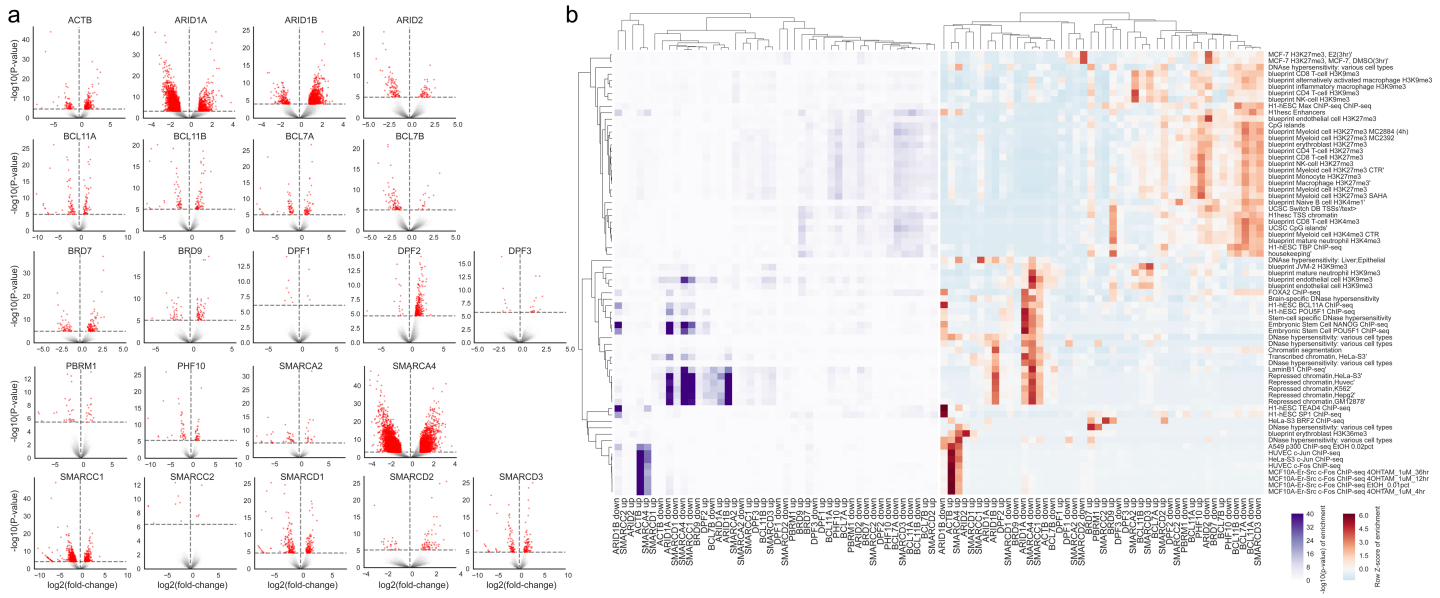

Supplementary Figure 7

Chromatin accessibility changes upon loss of single BAF subunits.

(a) Volcano plots showing the log2 fold-change (x-axis) in chromatin accessibility and its significance ($-\log_{10} P$ value; y-axis) for different HAP1 KO cells (KO is indicated on top) relative to HAP1 WT cells. Significance was calculated with a Wald test and FDR-based multiple comparison adjustment as implemented in the DESeq2 R package. (b) Enrichment of regions gaining- or losing accessibility in the different HAP1 knock-out cells relative to HAP1 WT cells in published ChIP-seq data from the ENCODE and Blueprint consortia, as determined by the location overlap analysis (LOLA) method. The left panel displays $-\log_{10} P$ value of a one-sided Fisher's Exact Test with no adjustment for multiple comparisons, while the right one shows a row Z-score of the same values.

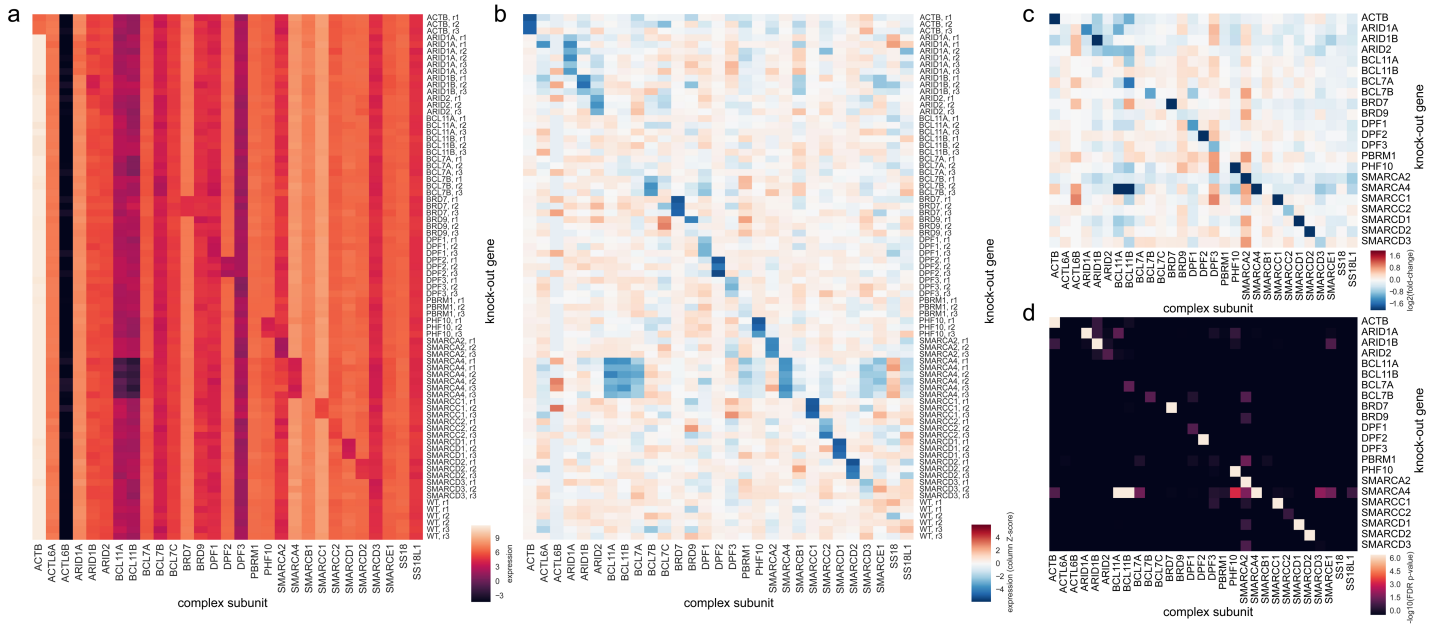

Supplementary Figure 8

Expression of BAF subunits across the different knock-out cells.

(a) Heatmap of gene expression (RNA-seq) for the different BAF subunits (x-axis) across the different HAP1 WT and KO cells (y-axis). (b) Same as in ˜(a), but with a row-wise Z-score. (c) Same as in (a), but showing fold-change to WT cells. (d) Same as in (c), but displaying significance of differential expression as assessed with the DESeq2 software using FDR-based correction for multiple testing. For all panels n = 3 biologically independent experiments.

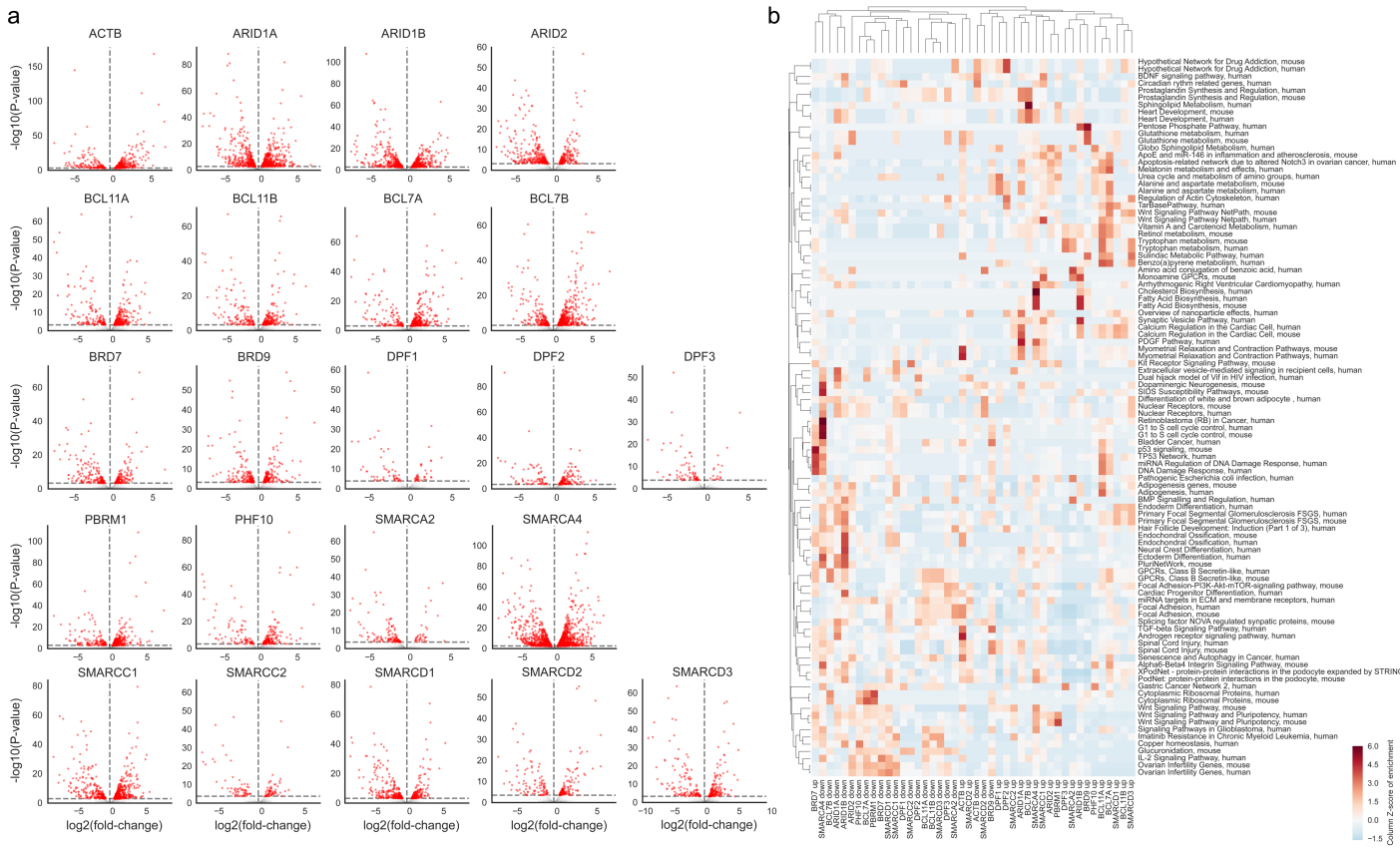

Supplementary Figure 9

Gene-expression changes upon loss of single BAF subunits.

(a) Volcano plots with $\log_2$ fold-changes of gene expression (x-axis) and their significance ($-\log_{10}$ *P* value; y-axis) for different HAP1 KO cells (KO is indicated on top) relative to HAP1 WT cells. Differential testing was assessed with the DESeq2 software and a *P* value without correction for multiple testing was displayed although genes were colored as significant depending on an FDR-based corrected *P* value. n = 3 biologically independent experiments were used. (b) Over-representation enrichment analysis of Gene Ontology terms in up- and down-regulated genes in the different HAP1 knock-out cells relative to HAP1 WT cells.

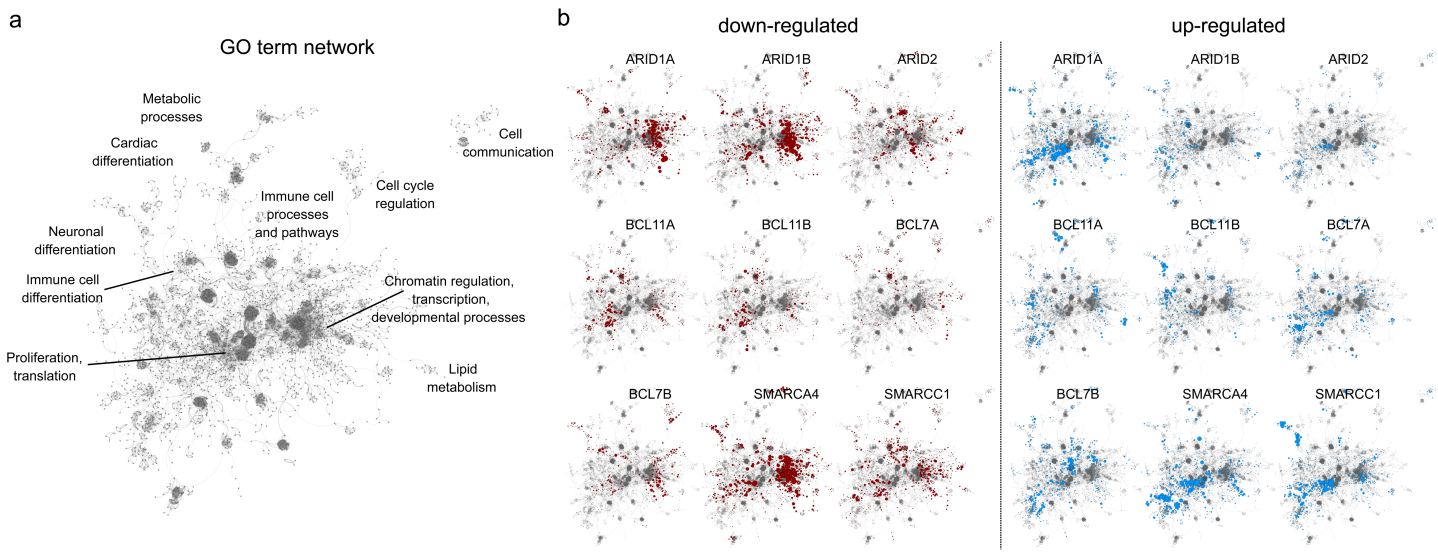

Supplementary Figure 10

Gene ontology networks show similarities in expression changes upon loss of single BAF subunits.

(a) Illustration of gene ontology (GO) term network. (b) Illustration showing which terms are associated with the down-regulated (red, left) or up-regulated (blue, right) genes of the indicated knock-out cells.

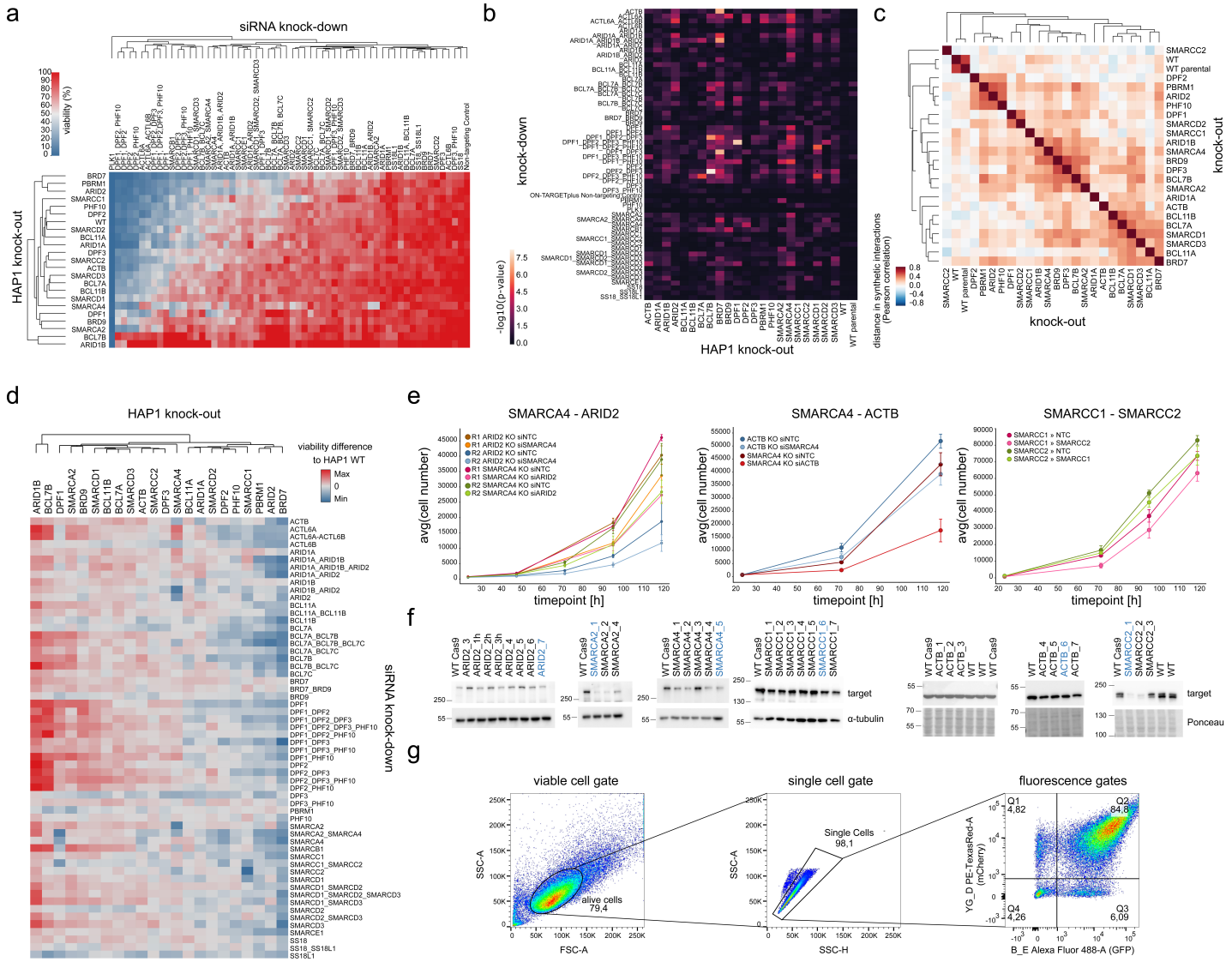

Supplementary Figure 11

BAF intra-complex synthetic lethalities.

(a) Heatmap showing the viability in the different HAP1 cells (y-axis, KO indicated) upon different siRNA knock-downs (x-axis, siRNA targets are indicated). Axes are clustered based on Euclidean distance measurement. (b) Heatmap with significance (-log$_{10}$ *P* value) of change in viability for different HAP1 knock-out cells (x-axis) compared to HAP1 WT cells upon siRNA knock-down (y-axis). *P* value was calculated by a two-sided t-test. (c) Pairwise Pearson correlation of different knock-out cells in their synthetic lethality pattern. (d) Heatmap showing the viability difference between the HAP1 knock-out cell lines (x-axis) and HAP1 WT cells upon siRNA treatment (y-axis). (e) Growth curves of HAP1 mutant cells after siRNA knock-down. Nuclei were counted after Hoechst staining (n = 3 individual samples, mean ± SD). (f) Western Blots testing knock-out efficiencies of different gRNAs per gene in HAP1 Cas9-expressing cells. Cells were selected with puromycin for 3 d before analysis. Blue labeled gRNAs were used for the multicolor competition assays. (g) Gating strategy for flow cytometry readouts of the multicolor competition assays.

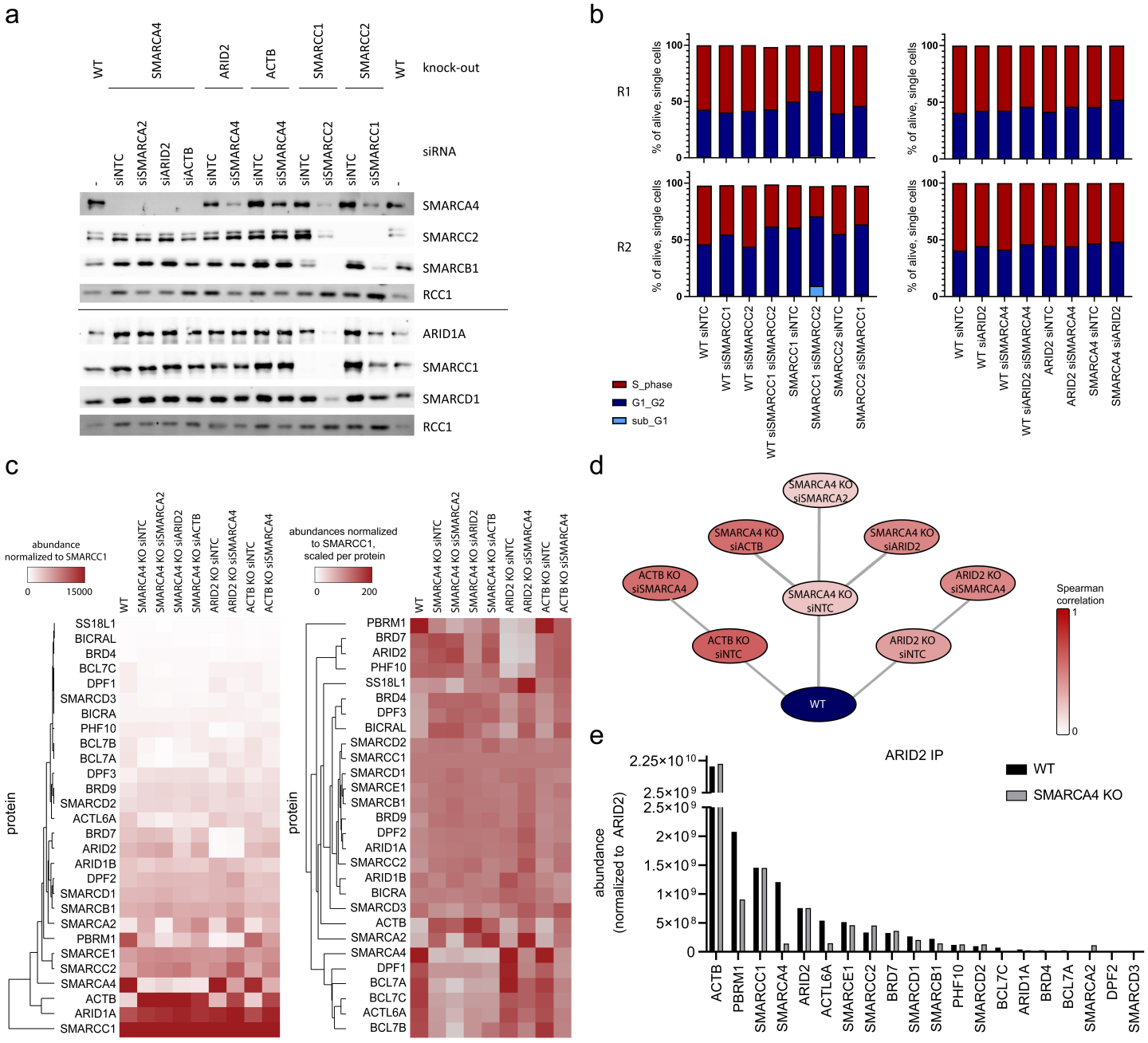

Supplementary Figure 12

Cellular and molecular consequences of BAF intra-complex synthetic lethalities.

(a) Western Blot of different BAF subunits 3 d after siRNA knock-down. (b) EdU cell cycle flow cytometer analyses 5 d after siRNA knock-down. (c) SMARCC1 IP-MS 3 d after siRNA knock-down in HAP1 mutant cells (n = 2 biologically independent experiments). Average abundance normalized to SMARCC1 is shown on the left. The abundances are scaled per protein on the right. UPGMA method was used for clustering with Euclidean distance measure. (d) Spearman correlation between measured protein abundance ratios in KO-siRNA experiments over WT and values predicted based on the interaction network constructed from the SMARCA4 and ARID1A IPs displayed in Supplemental Fig. 2f (blue part). Sample size can be found in the Supplementary note. (e) Abundance of BAF genes in HAP1 WT and SMARCA4 KO cells after ARID2 IP-MS. The abundances are normalized to ARID2.

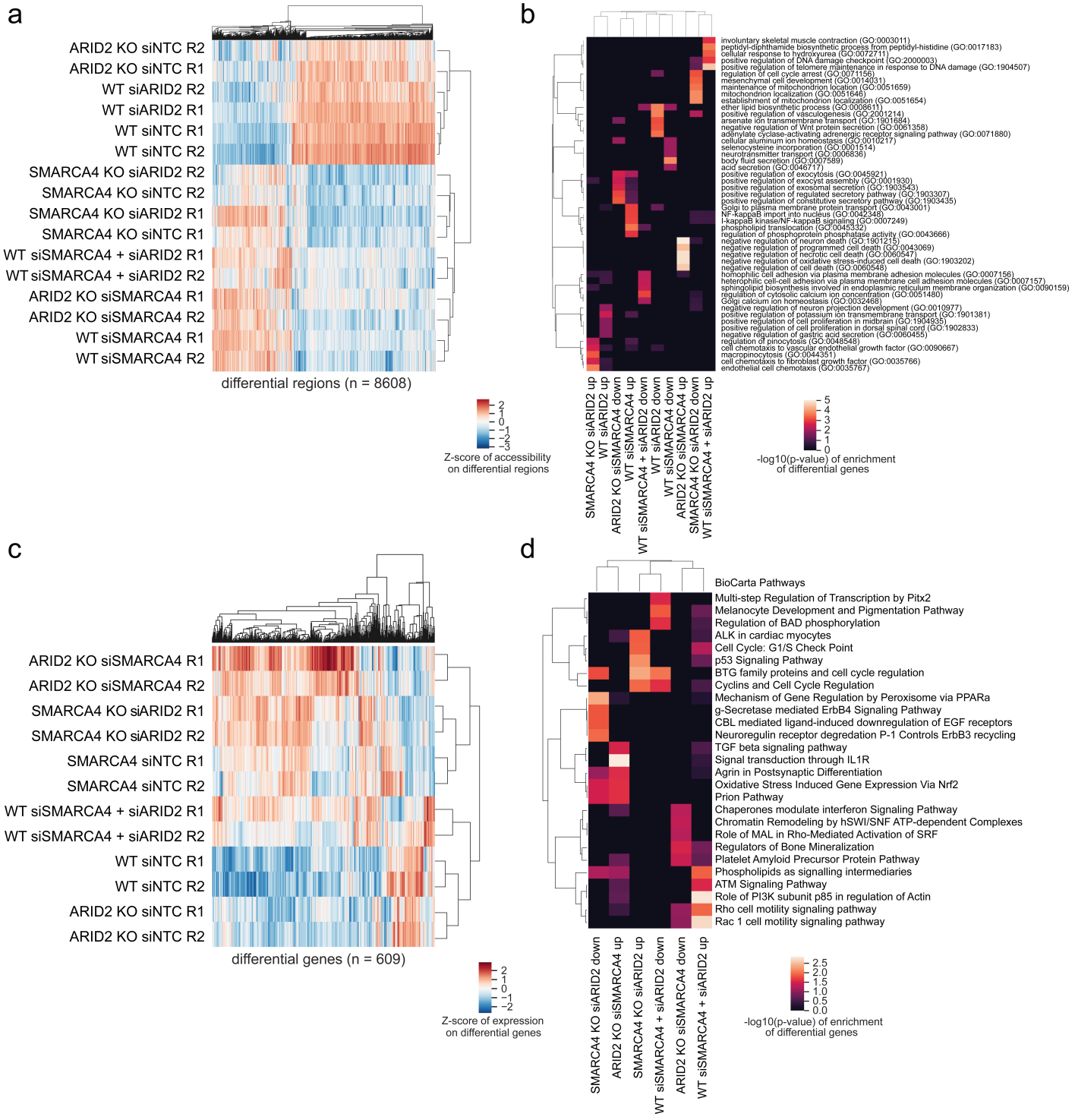

Supplementary Figure 13

Chromatin and gene expression alterations in BAF intra-complex synthetic lethal conditions.

(a) Heatmap showing differential ATAC-seq regions 5 d after siRNA treatment. (b) Enrichment of genes associated with differential ATAC-seq regions in Biological Process terms from Gene Ontology. (c) Heatmap showing differentially expressed genes determined by RNA-

seq 5 d after siRNA treatment. (d) Enrichment of differentially expressed genes in pathway terms from BioCarta. For panels (b) and (d) significance was assessed with a one-sided Fisher's Exact Test without correction for multiple testing. n = 2 biologically independent experiments were used for ATAC-seq and RNA-seq.

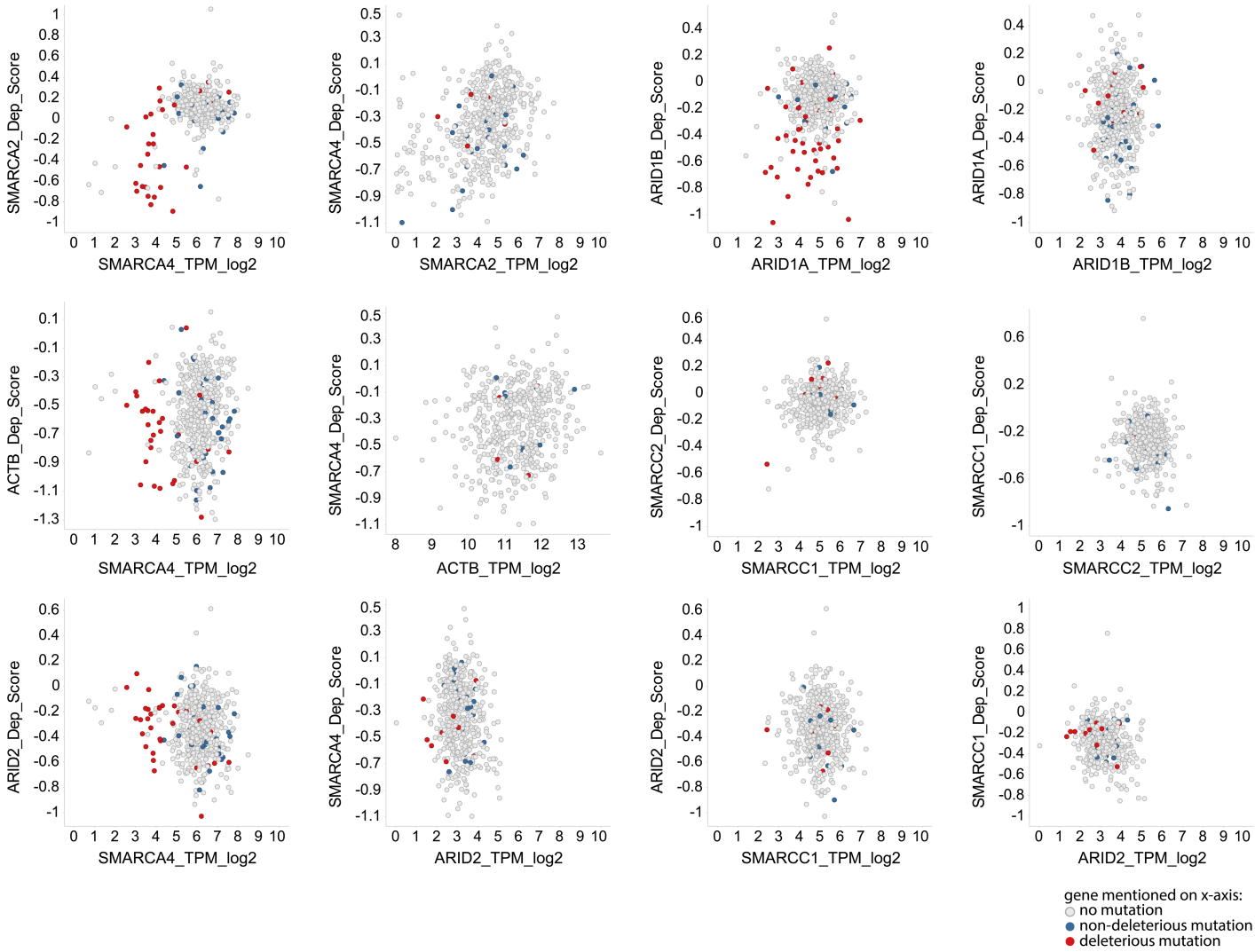

Supplementary Figure 14

Analysis of BAF-dependencies using public data.

CRISPR dependency score when targeting indicated BAF gene (y-axis) versus expression of another BAF gene (x-axis) in various cell lines (depmap: CRISPR (Avana) Public 18Q4).

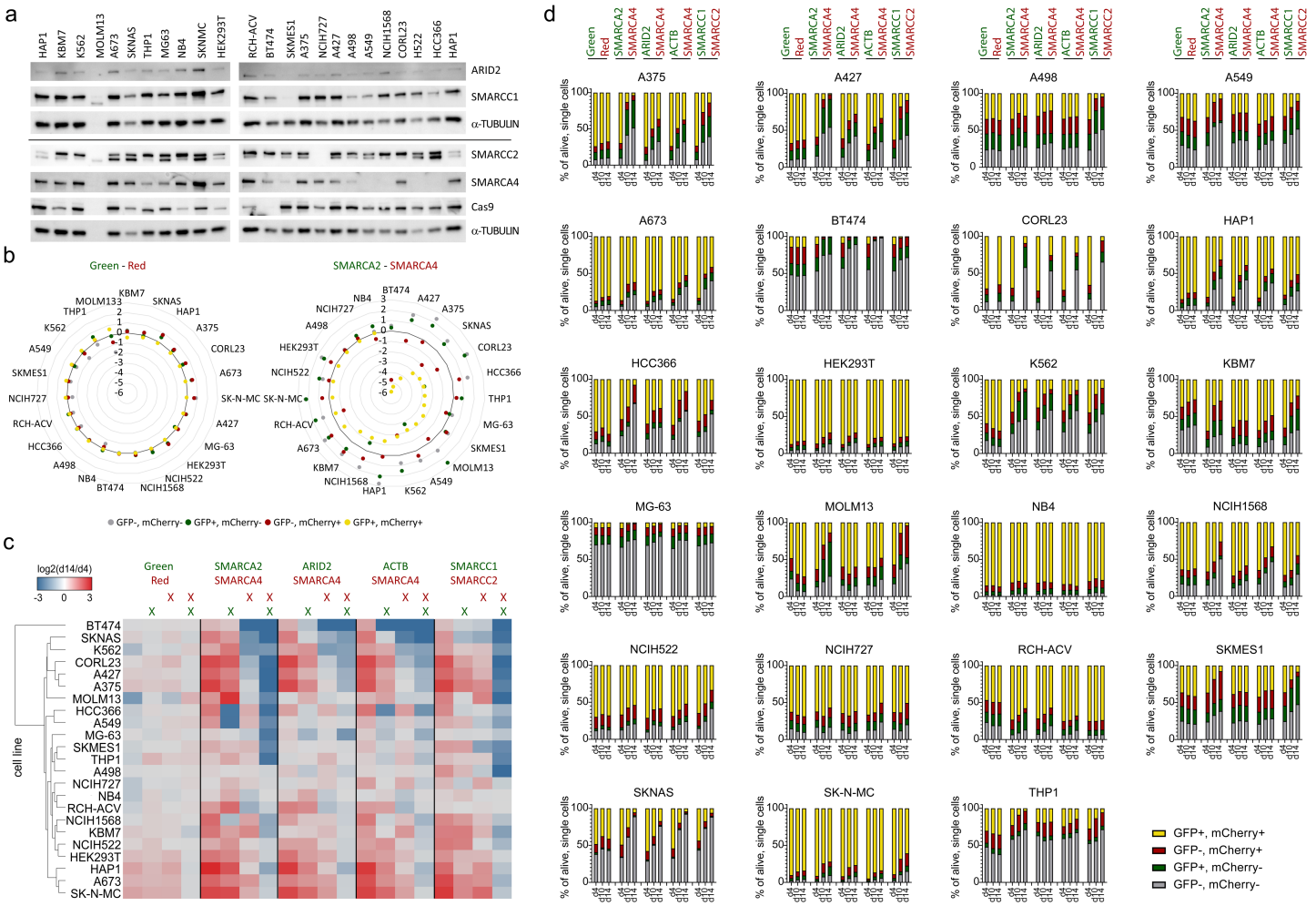

Supplementary Figure 15

Intra-complex synthetic lethalities across various cell types.

(a) Western blots showing expression of selected BAF subunits and Cas9 in cell lines used for multicolor competition assay. α-TUBULIN serves as a loading control. (b) Results of the positive and negative controls from the multicolor competition assays. $\log_2$(d14/d4) are displayed. Targeted subunits are indicated above (Green, Red: vectors only with the fluorescent marker). (c) Heatmap showing the $\log_2$(d14/d4) results of the different cell lines in the multicolor competition assays. Cell lines are clustered based on UPGMA method with Euclidean distance measure. (d) Stacked bar graphs showing the percentage of the four populations measured by flow cytometry over the time-course of the multicolor competition assays. Cell lines are indicated above the graphs. Targeted subunits are indicated on the top (Green, Red: vectors only with the fluorescent marker).